Magnetic Resonance in Chemistry

WILEY

RESEARCH ARTICLE OPEN ACCESS

MRI for Mixing Quality in Microfluidics

J. Götz[1] | T. Rudszuck[1] | L. Kontschak[1] | T. Oerther[2] | H. Nirschl[1] | G. Guthausen[1,3]

[1]Institute of Mechanical Engineering and Mechanics, KIT, Karlsruhe, Germany | [2]Bruker BioSpin GmbH & Co. KG, Ettlingen, Germany | [3]Engler-Bunte Institut, Water Science and Technology, KIT, Karlsruhe, Germany

Correspondence: G. Guthausen (gisela.guthausen@kit.edu)

Received: 5 January 2026 | **Revised:** 25 February 2026 | **Accepted:** 28 February 2026

Keywords: chemical shift imaging | mixing quality | MRI | NMR | paramagnetic relaxation enhancement | process monitoring

ABSTRACT

Liquid state processes often involve mixing of process streams. With the development of microfluidics in chemical engineering, questions arise about analytical tools which are capable of monitoring the processes spatially and time-resolved. Optical techniques are widely spread, which, however, require optical transparency. MRI techniques are explored to elucidate the possibilities of measuring hydrodynamic parameters and monitoring mixing with molecular, chemical information.

1 | Introduction

MRI provides a variety of non-invasive and non-destructive methods to monitor the progress of reactions and processes, also on the length scale of microfluidic devices—here with the focus on liquids in an example y-micromixer. As magnetic resonance is a rather insensitive analytical tool due to the small energy gap between nuclear spin levels, one main issue in this context concerns sensitivity which directly determines resolution—in the context of monitoring time evolving processes via MRI, time as well as spatial resolution [1, 2]. Sophisticated technical approaches mainly concern radio frequency (rf) microcoils and electric circuits [3–12]. Signal enhancement methods are known, including dynamic nuclear polarization (DNP) and chemically specific enhancement strategies like SABRE (signal amplification by reversible exchange) and CIDNP (chemically induced DNP) [13–16]. Less specific approaches are known, among which paramagnetic relaxation enhancement (PRE) needs to be mentioned. For example, T_1-contrast agents reduce longitudinal relaxation of nearby substances to be observed [17–19]. In consequence, and from the perspective of process monitoring of flowing liquids, these agents effectively shorten the polarization length at a given flow rate. Therefore, flow can be faster while still reaching the thermal magnetization equilibrium on one hand; on the other hand, the repetition time of the NMR/MRI experiments can be shortened accordingly. In short, by tweaking in- and outflow effects, the optimal signal-to-noise ratio provides the basis for reliable process observation [2, 20, 21], with and without PRE agents. Even more, when knowing the relaxation times in the liquid mixtures, back-calculations still allow the quantitation of reaction progress in the case of sub-thermal polarization [22].

In this paper, MRI techniques were applied to measure and derive mixing quality in an example microfluidic device in the form of a static mixer. A recent review thereby summarizes the aspects of hydrodynamics [23]. Mixing was studied in such a static mixer, exploring PRE and chemical shift imaging, both techniques with their specific view on the mixing progress along the fluidic path of the device.

2 | Experimental

2.1 | Experimental Setup for the MRI Measurements on a Microfluidic Mixing Device

MRI experiments were performed on an Avance Neo 400 MHz spectrometer equipped with a wide bore magnet (9.4 T) and microimaging accessories. The MRI signals were recorded within the Bruker software Paravision 360 (Table 1). *x*,*y*,*z*-gradients for spatial resolution were provided via Great 60 amplifiers. A

TABLE 1 | Acquisition parameters for ^{1}H MRI measurements.

		Pulse sequence and values				
Parameter	**Unit**	**RARE**	**FLOWMAP**	**MSME tagging**	**PRESS**	**FLASH**
Repetition time t_R	[s]	0.4	1.5 (Figure 2) 0.6 (Figure 4)	0.13	0.8	0.15
Echo time τ_e	[ms]	6	5.92	5	13.8	5
RARE-factor	[–]	3	—	—	—	—
In plane field of view	[mm × mm]	9.6 × 1.8	9.6 × 1.8	1.8 × 1.8	—	1.8 × 1.8
Data matrix size	[px × px]	256 × 48	256 × 48	96 × 96	128	112 × 112
In plane voxel size	[μm × μm]	37.5 × 37.5	37.5 × 37.5	18.75 × 18.75	600 × 250	16 × 16
Slice thickness	[mm]	0.19	0.2	0.12	0.1	0.15
Number of averages	[–]	8	8	32	128	32
Measurement time	[min]	3	19.2 7.7	5.1	1.7	6.9

maximum gradient of 3 T/m was thus realized using a micro5 gradient. The radiofrequency probe was a Diff30 probe equipped with a 1.7 mm rf coil in which the microfluidic mixer was placed [24]. The sensitive length of this coil along z is 8 mm. All devices were provided by Bruker BioSpin GmbH & Co. KG, Ettlingen, Germany.

As MRI pulse sequences, RARE (rapid acquisition with relaxation enhancement) and PRESS (point-resolved spectroscopy, a double spin-echo pulse sequence of 90°–180°–180° with slice-selective pulses for spatial encoding of voxels) were applied, resulting in relaxation-weighted images and spatially resolved spectra with chemical shift resolution as a basis for quantification of mixing quality. In addition, the velocity field was measured via MSME (multi-slice multi-echo) tagging and FLOWMAP, revealing the fluids' velocities $v_x(\boldsymbol{r})$, $v_y(\boldsymbol{r})$, $v_z(\boldsymbol{r})$, depending on the spatial coordinate $\boldsymbol{r}$.

2.2 | Experimental Setup of the Microfluidic Mixing Device

As an example of a microfluidic mixing device, a y-mixer was 3D printed (printer Keyence Aglista series 3000, material: AR-M2, Figure 1). A special geometric requisite was that the fluidic channels meet only after 36 mm in order to be able to observe the mixing of the two streams by MRI directly from the merging point along the fluidic path. Other material and geometric constraints were given by the MRI setup, leading to a total length of the small-scale device of > (61 + 36) mm, which is a considerably large length for a 3D printed polymeric device. These constraints made printing demanding—on account of accuracy. A technical drawing of the device is given together with a photograph in Figure 1, which shows the two fluidic paths with cross-sections in the order of 300 μm × 700 μm, merging into one channel (600 μm × 700 μm) after $z = 36$ mm. The mixing device needed to be connected to the supplying fluid streams delivered by micro-tubes (inner diameter 150 μm), which was realized by micro-chromatographic connectors. The micro-tubes were threaded through the tempering channel in the Diff30 probe, normally equipped with a glass dewar. The dewar was removed to make the fluidic path into and out of the magnet and probe as short as possible with a positive side effect on the handling of the experimental setup. Fluidic streams were provided by a syringe pump (kdScientific KDS-210-CE) equipped with two places for syringes such that an identical forward-acting feed rate leads to individual volume rates and velocity profiles in the fluidic paths. For identical syringes, equal flow rates of both channels are realized (configuration K_1), which were always in the laminar flow regime with Reynolds numbers in the order of 1. Syringes differing in volume lead to different, but well-defined volume flow rates (configuration K_2, here a factor of 2, see below). The connection between the syringes and the PTFE micro-tubes was realized via Luer-adapters.

3 | Results and Discussion

3.1 | Velocity Maps in the Y-Mixer: Water – Water and Ethanol - Aqueous Saccharose Mixing

Mixing of fluids is determined by velocity $\boldsymbol{v}(\boldsymbol{r}) = (v_x(\boldsymbol{r}), v_y(\boldsymbol{r}), v_z(\boldsymbol{r}))$, among other factors as viscosity or diffusion. The velocity vector was therefore measured spatially resolved in the y-mixer on water with contrast agent (Figure 2). The coronal slices (slice selection along x, whereas y and z provide the image plane) for all three velocity components show the expected behavior: at the inlet ($z < 2$ mm), pronounced v_y velocities were observed in the two channels. v_y shows negative and positive velocities which reflect the flow direction projected onto the y axis. Please note the numbers on the false color scale, which make the difference between the transverse velocities (v_x, v_y) and the longitudinal velocity along z evident. v_z is largest at the inlet in the two channels ($z < 2$ mm) because of channel sizes. At $z > 2$ mm, the transverse velocities are small, and the main flow direction is along z. Laminar behavior as described by the Hagen–Poiseuille law was approximately observed in the quantitative analyses of flow maps as well as in MSME tagging experiments (not shown). This

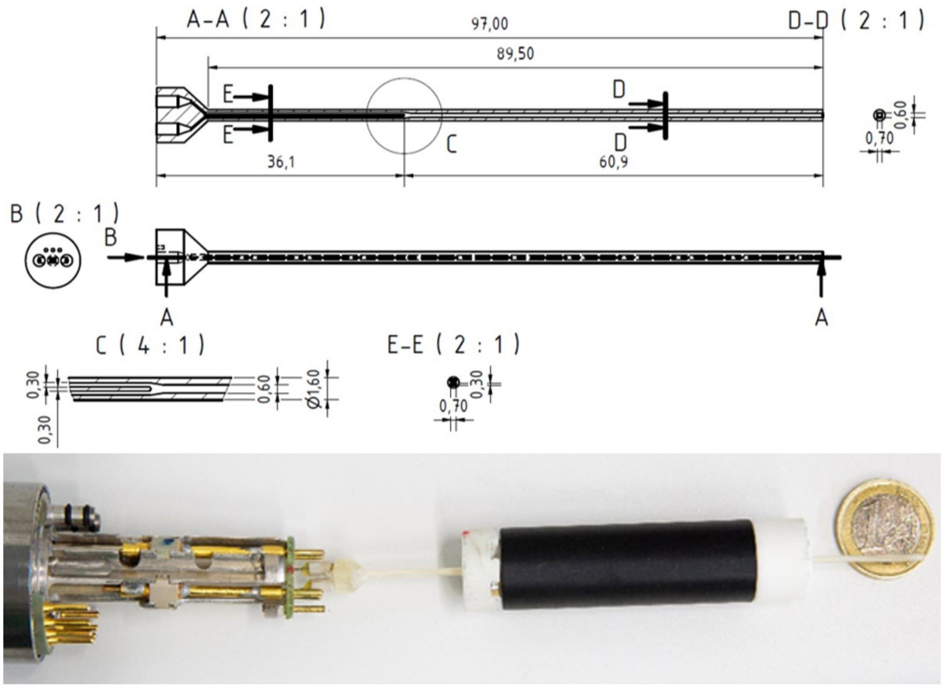

FIGURE 1 | Top: Drawing of the y-mixer studied as an example of a microfluidic device. Please note the long entrance length of the two channels which allowed MRI measurements at the merging point (C) in the mixing device. Bottom: The 1.7 mm rf coil was designed as insert for a Diff30 probe. The micromixer was mounted inside the coil.

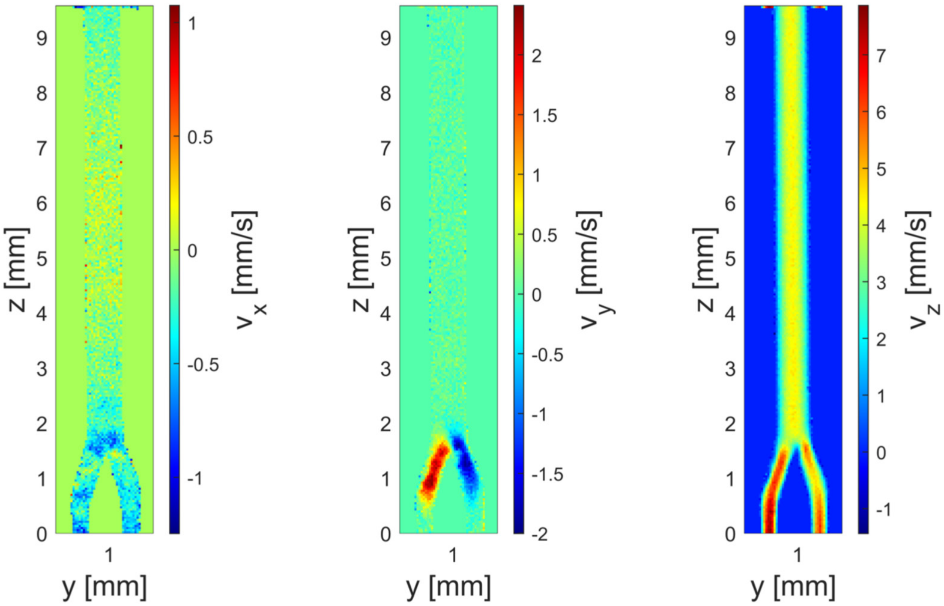

FIGURE 2 | Velocities as measured by FLOWMAP in a coronal slice showing the velocities in the two channels before the merging point and in the mixing channel at $z > 2$ mm. Please note the positive and negative velocities v_y as well as the different false color scales of the velocity components.

finding is consistent with the values of the Reynolds numbers in all presented experiments. Of course, the mixer's geometry and printing imperfections on the scale of $< 50\,\mu$m influence the velocity field, apart from the pump's pressure and fluid properties, and cause small deviations from the theoretical description.

A common situation is the mixing of fluids with different properties, for example with different macroscopic dynamic viscosities η and different diffusion properties. These properties have a pronounced impact on the flow fields and consequently on the mixing process itself. As an example, aqueous ethanol (mass ratio $w_{\mathrm{EtOH}} = 0.38$, viscosity $\eta = 2.2$ mPa·s at temperature $T = 295$ K) in one channel and aqueous saccharose solution ($w_{\mathrm{S}} = 0.333$, $\eta = 3.6$ mPa·s at $T = 295$ K) in the other channel met in the y-mixer; both liquids contained 1 mmol/L Gadovist for reduction of longitudinal relaxation time and consequently measurement time. Primarily, the question about stationary flow fields needs to be answered. It was addressed via tagging, applying a MSME sequence with the parameters summarized in Table 1.

The sagittal images (Figure 3A,B) nicely show the deviation from the Hagen–Poiseuille behavior, expected for a one-phase laminar flow in a cylindrical tube. The coronal images (Figure 3D,E) reflect the stationary flow in a plane which is not directly involved in mixing. In a first experiment (Figure 3A,D), the volume flow of both channels was equal (configuration K$_1$), leading to a total mass flow rate of $\dot{M}_1 = 0.1\,\mathrm{g/min}$. In the second case,

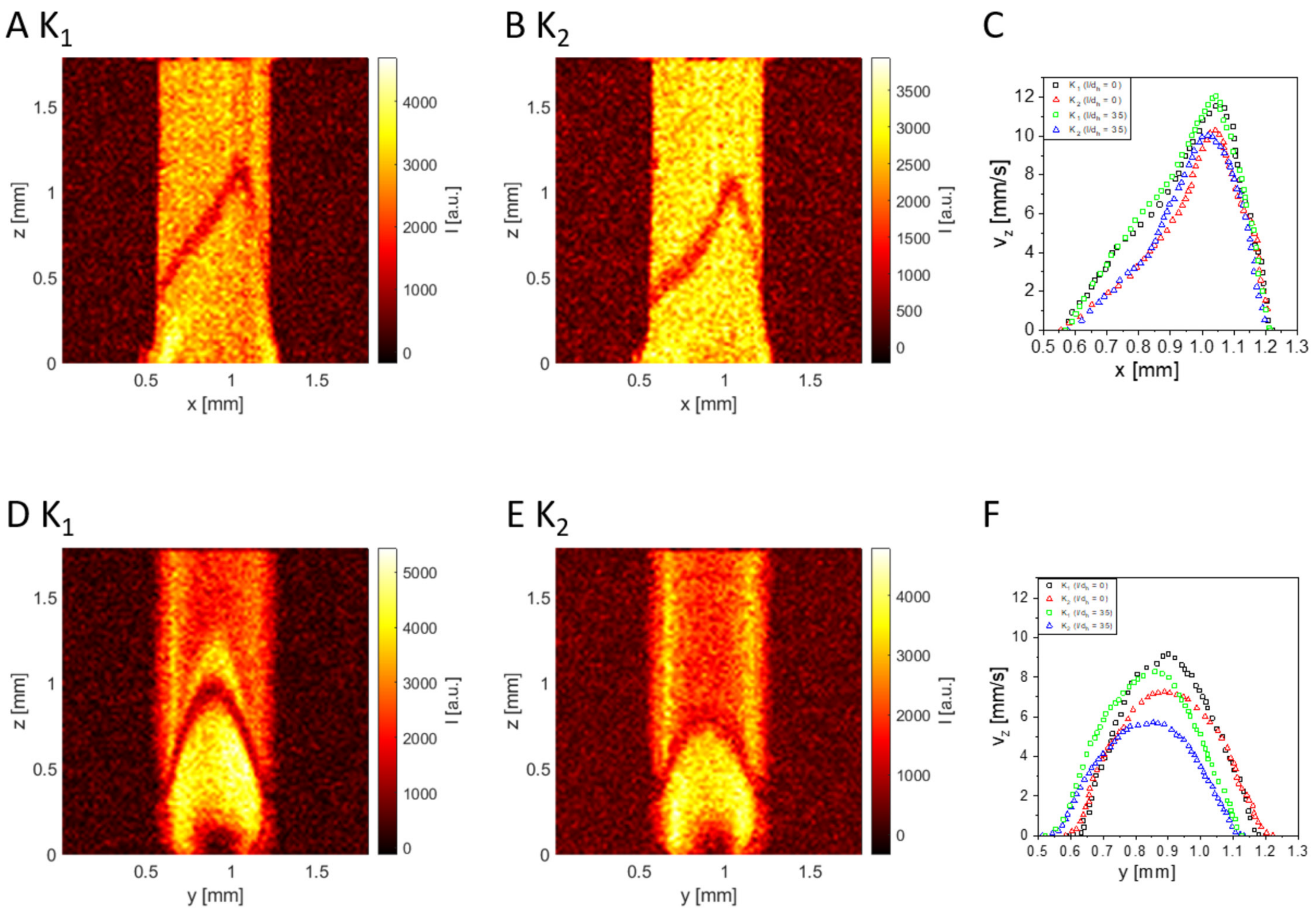

FIGURE 3 | Tagging in a MSME experiment shows the impact of viscosity on the velocity field near the merging point of the two fluids, here on the example of mixing aqueous ethanol/saccharose solutions. Saturation stripes show the expected pronounced deviation from the Hagen–Poiseuille law: (A, B) sagittal slices, (D, E) coronal slices, whereas (A, D) were measured with configuration K$_1$, (B, E) with configuration K$_2$. (C) and (F) show the velocity profiles of v_z, the z-component of the velocity for K$_1$ and K$_2$, respectively. The deviation from the Hagen–Poiseuille flow becomes evident, especially in the sagittal measurement geometry (A, B).

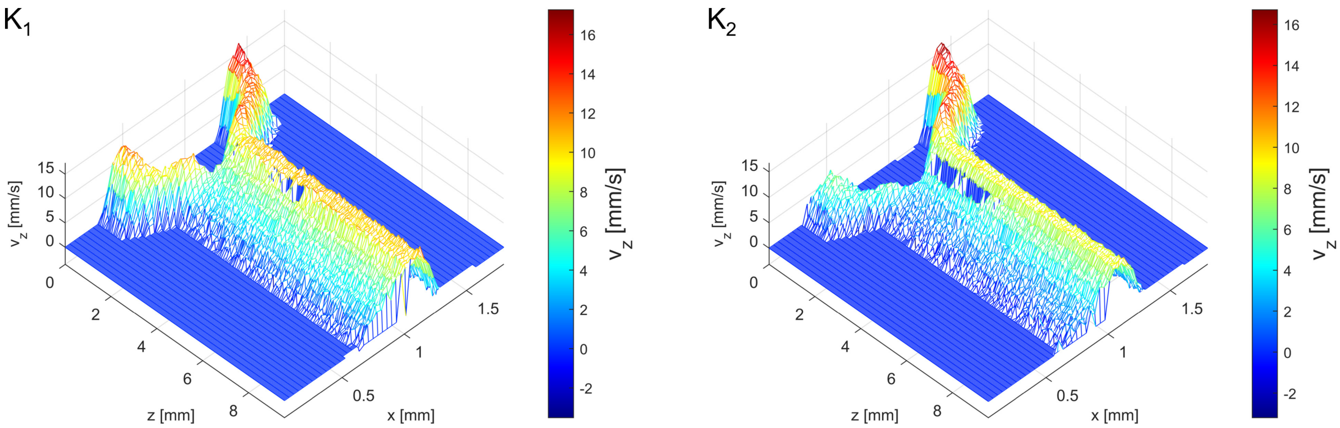

FIGURE 4 | The velocity component v_z was measured by FLOWMAP for both configurations $\mathbf{K_1}$ and $\mathbf{K_2}$, on aqueous ethanol and sucrose solutions with differing viscosities. Please note the asymmetric velocity distributions at merging of the two channels ($z \approx 1.5\,\mathrm{mm}$), especially pronounced in configuration $\mathbf{K_2}$, which are determined by the flow rates and viscosities as well as by the mixing properties of the two streams.

K_2, the volume flow of the first syringe containing the saccharose solution was halved (Figure 3B,E), such that the total mass flow rate amounted to $\dot{M}_2 = 0.075\,\text{g/min}$. Velocity profiles were calculated from sagittal and coronal slices, whereas the position along z was varied denoted by the ratio l/d_h ($l/d_h = 0$, black and red data points and $l/d_h = 35$ in green and blue, Figure 3C,F). d_h is the effective radius of the mixing channel and amounts to $0.35\,\text{mm} \pm 0.03\,\text{mm}$. l is the distance along z, whereas $l = 0\,\text{mm}$ denotes the merging point of the two channels. The velocity profiles are asymmetric, which clearly is a result of the fluids properties. The channels and mixing geometry as well as the flow distance also contribute, as becomes evident in the coronal and sagittal images.

Apart from tagging, flow fields were investigated via FLOWMAP (Table 1). The velocity along the long axis of the mixer, v_z, was measured (Figure 4). The maps nicely show the approach to equilibrium velocity downstream of the merging point. The rule of thumb that the velocity field approximates equilibrium latest after 10 times the tube's inner diameter was confirmed. As the inlet flow rates differ in configuration K_2, the imbalance at the merging point becomes more evident ($z < 5\,\text{mm}$). The velocity maps are in accordance with the findings in the tagging experiments.

3.2 | Mixing by Exploiting Relaxation Contrast

As well known, mixing of fluids depends not only on velocity fields and channel properties like surface roughness but also on the fluids material parameters like diffusion, viscosity and hydrophobicity. In a first approach, these parameters were constant, water was used: one channel was fed with water containing Gadovist (GDV, initial concentration $c_{GDV} = 1\,\text{mmol/L}$), the other channel was fed with pure demineralized water. The hydrodynamic parameters consequently are the same for both feeds, whereas the MR image contrast was here given by longitudinal relaxation, which allows to determine the mixing quality along only the longitudinal relaxation rate R_1. The concentration of the contrast agent can be derived spatially resolved, as it is linearly correlated with R_1 via the material specific relaxivity r_1. At 400 MHz, Gadovist in water provides a longitudinal relaxivity $r_1 = 0.37 + 4.54\ c_{GDV}$ (unit: [L/(mmol*s)]), whereas $c_{GDV} \in [0,1]\,\text{mmol/L}$. Thereby, Gadovist is a paramagnetic cluster inducing dominantly longitudinal PRE on ^{1}H spin relaxation of neighboring molecules, here water. In consequence, mixing efficiency is reflected in the Gadovist concentration c_{GDV} deduced from R_1 weighted MR images.

In a first step, R_1 weighted images were measured by RARE (Table 1, Figure 5) at two different pumping speeds, which of course influence mixing as the residence time of a voxel depends on the voxel's velocity and therefore also the effective mean free path length of diffusion.

Already the T_1 weighted images show mixing for both configurations by blurring colors. The mixing efficiency becomes more evident in the maps of the Gadovist concentration which were calculated from the amplitude images taking into account the longitudinal relaxivity. Perfect mixing, that is, $c_{GDV} = 0.5\,\text{mmol/L}$ (green on the false color scale) in each voxel, is only observed in the middle of the mixing channel for both configurations. Deviations occur in a more pronounced manner towards the surfaces of the y-mixer, while twisted streaming was also observed. Not shown is the situation at the merging point for larger volume flow rates which indicates lower mixing efficiency due to more pronounced channeling.

3.3 | Mixing by Exploiting Chemical Shift Differences

Not only can relaxation contrast be exploited to measure concentrations and mixing quality in a spatially and time-resolved manner, but foremost chemical shift. Several pulse sequences are known in MRI, for example chemical shift imaging, involving spatial encoding by phase gradients. Localized

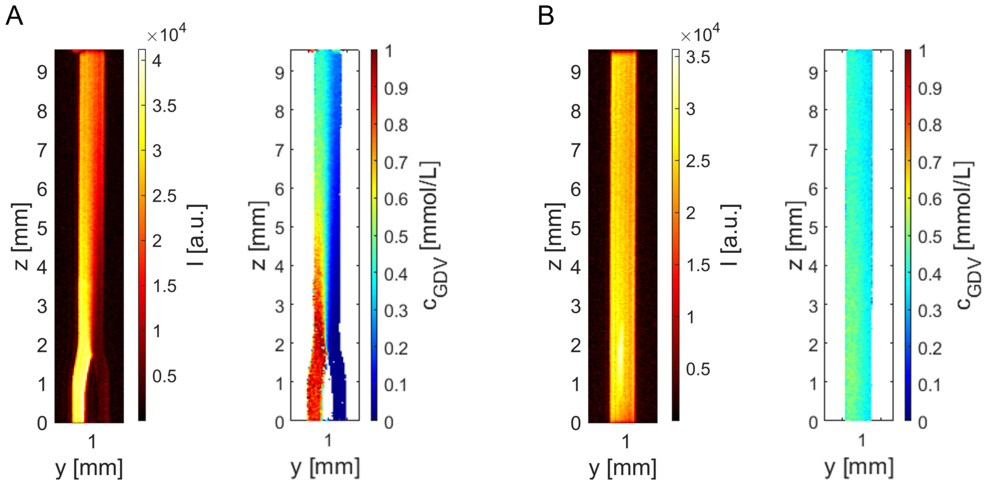

FIGURE 5 | T_1 weighted images reveal the concentration of Gadovist. (A) T_1 weighted signal amplitude at a small pumping rate, at the inlet and merging point of the two channels, and the corresponding concentration map $c_{GDV}(y,z)$ on a different false color scale (jet instead of hot iron). (B) T_1 weighted image in the mixing channel at $l/dh = 35$ and a volume flow rate of a factor 10 larger. The corresponding relative concentration map still shows non-ideal mixing with $c_{GDV} \neq 0.5\,\text{mmol/L}$.

spectroscopy in form of PRESS was applied here to study mixing quality using molecular signatures in relatively simple mixtures on the example of a y-mixer. This approach allowed to measure localized NMR spectra in flow. This provides information about mixing of flowing liquids in the microfluidic device which is optically opaque as a result of 3D printing. The voxel size was 0.1 mm × 0.25 mm × 0.6 mm (Figure 6A) in the first example of mixing water with aqueous ethanol, whereas the viscosities of the two fluids are different. Both liquids contained the contrast agent Gadovist for reducing T_1. The data were recorded under stationary hydrodynamic conditions. At the merging point ($l/d_h = 0$), almost no mixing was observed as expected. The situation changes with increasing l/d_h along the *z*-axis which coincides with the long axis of the mixer. As obvious in Figure 6A near the outlet of the mixer, the relative signal intensities vary along *x*. The FLASH image thereby contained the mixing plane. It gives also a first indication about the heterogeneity of the mixing quality, which is reflected in the PRESS images (Figure 6A). When measuring PRESS along *z* in a next step, the mass fraction of ethanol, w_{EthOH}, can be calculated as a function of *x* and implicitly as a function of *z* and l/d_h, respectively (Figure 6B). The mean mass fraction of ethanol is $\overline{w}_{\mathrm{EtOH}} = 0.184$ in this experiment and is observed in the middle of the channel as expected.

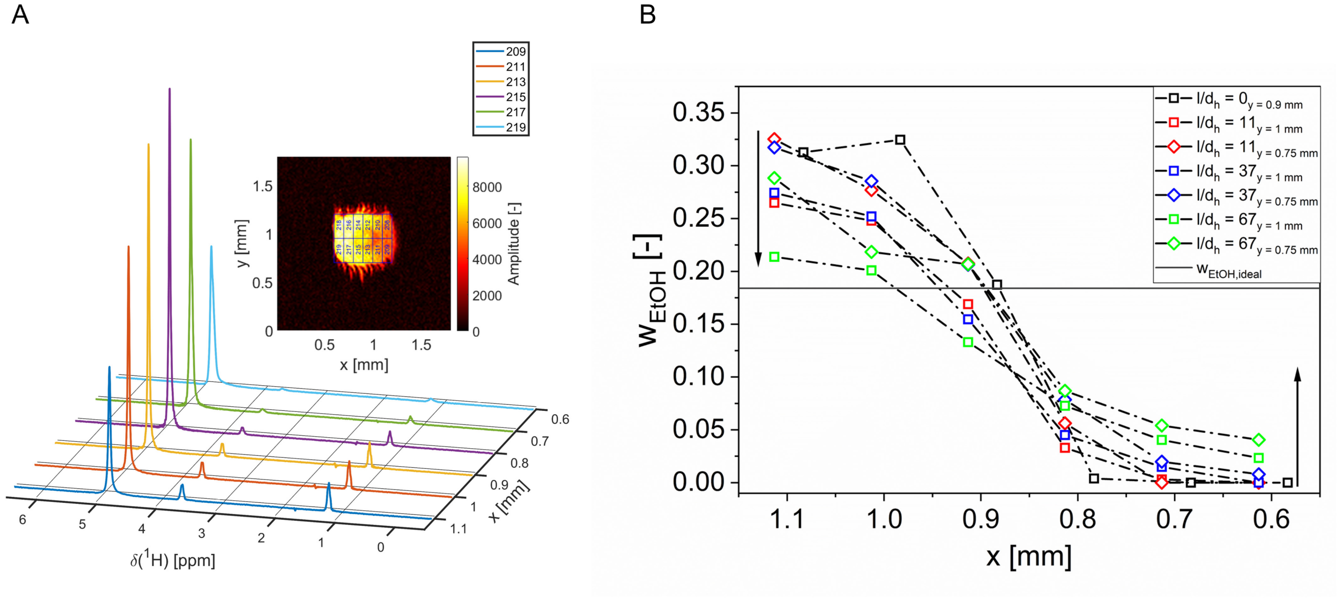

FIGURE 6 | Localized spectroscopy (PRESS) on the y-mixer at $l/d_h = 67$ (A). The voxels are defined in the axial FLASH image at two values of *y*, respectively. The spectra, although not J-coupling resolved, allow the assignment to the involved molecules; the integrals deliver the relative concentration in the given volume element and finally the mass fraction of ethanol (B), which was derived as an implicit function of l/d_h. The straight line symbolizes ideal mixing in the given experiment.

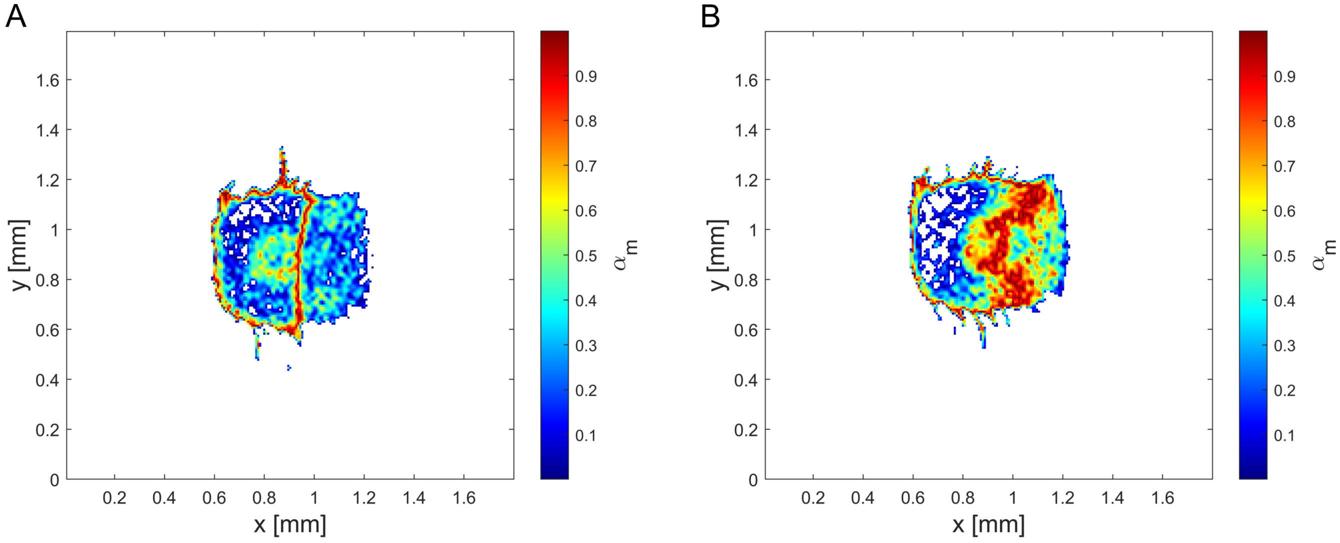

FIGURE 7 | Axial slices of calculated mixing quality under flow at (A) $l/d_h = 0$, the merging point of the two channels, (B) $l/d_h = 67$ near the outlet of the mixer. Although (A) shows a sharp transition characterized by $\alpha_m \in [0, 1]$ between the two liquids, (B) shows a large area of good mixing although areas of low and almost pure liquids are observed, especially at smaller *x* which corresponds to the water inlet.

3.4 | Data Analysis of MRI Data — Calculation of Mixing Quality Maps From MR Images

The established quality parameter in mixing processes is the mixing quality α_m, which is defined according to [23, 25, 26] in the case of mixing of water and ethanol:

$$\alpha_m = 1 - \sqrt{\int \left(w_{\mathrm{EtOH}} - \overline{w}_{\mathrm{EtOH}}\right)^2 \mathrm{d}A / \left(\overline{w}_{\mathrm{EtOH}} * \left(w_{\mathrm{EtOH,max}} - \overline{w}_{\mathrm{EtOH}}\right)\right)}$$

$\alpha_m \in [0, 1]$, from completely unmixed to completely mixed. This formula can of course be generalized to the mixing of liquid A and B. α_m can thus be calculated from w_{EtOH} (Figure 6B) of the PRESS spectra—with the limited spatial resolution compared with FLASH images. Nevertheless, the variation in concentration is evident in the spectra within the axial slice. FLASH images, however, also show an image contrast depending on w_{EtOH} and consequently contain the information about mixing quality which needs to be quantified accordingly. When correlating the image intensities with w_{EtOH} from PRESS, FLASH images can be transferred into α_m maps just by calculating $\alpha_m(\boldsymbol{r})$ from $I(\boldsymbol{r})$ along that correlation (Figure 7). The numerical parameters of the correlation equation, often in form of a linear relation, of course depend on the properties of the mixing fluids, on hydrodynamics and on MRI parameters. Hence this calibration of signal amplitudes is not unique, whereas the approach is. A nice property of this approach additionally is that the correlation can be established by a multitude of data points along the concentration axis which provides improved statistical reliability and accuracy.

The described approach was also used to analyze the mixing behavior of an aqueous sucrose solution and ethanol at different relative volume flow rates, which increased the difficulties on the one hand regarding the hydrodynamic properties and their differences of the two fluidic streams, on the other hand regarding the quantification of the NMR spectra due to multiple lines and partial line overlap. Nevertheless, the mixing quality maps were calculated also in that setup and showed the expected behavior. This assures that the described approach can be transferred to more complicated mixing fluids and geometries flowing through a microfluidic device.

4 | Conclusion

On the small length scale of microfluidic devices, the NMR sensitivity becomes a limiting factor. Apart from signal hyperpolarization methods, an optimization of the rf field B_1 allows time and spatially resolved monitoring of processes under flow, also combined with longitudinal PRE. This is demonstrated here on the example of a simple y-mixer fabricated by 3D printing and being optically opaque.

Mixing directly at the merging of fluidic streams could be detected by making use of longitudinal PRE, which primarily reduced the longitudinal relaxation time and generated a contrast between the two flowing fluids to be mixed in the laminar flow regime. Second, chemical shift and its specificity to chemical functional groups were explored, which allowed monitoring mixing in a microfluidic device with a channel dimension of $600\,\mu\mathrm{m} \times 700\,\mu\mathrm{m}$. Quantitation was made in the form of maps of mixing quality, also by combining the good spatial resolution of FLASH with the concentration map obtained by chemical shift resolved PRESS.

As an outlook, signal enhancement strategies will be applied such as various forms of hyperpolarization and PRE for improving time resolution and—if required—spatial resolution down to the diffusion limit.

Acknowledgements

The authors thank the μ-imaging group at Bruker BioSpin GmbH for their support during this work, as well as the Deutsche Forschungsgemeinschaft (DFG) for providing NMR instrumentation and funding within the Pro^{2}NMR facility. Financial support from DFG for the project within the CRC Hyperion is also gratefully acknowledged: Project-ID 454252029 - SFB/CRC 1527. The authors thank the workshop staff for their assistance during construction.

Funding

This work was supported by Deutsche Forschungsgemeinschaft (instrumental facility and Project-ID 454252029 - SFB/CRC 1527).

Conflicts of Interest

The authors declare no conflicts of interest.

Data Availability Statement

The data that support the findings of this study are available from the corresponding author upon reasonable request.

References

1. R. Kimmich, *NMR—Tomography Diffusometry Relaxometry* (Springer Verlag, 1997).

2. P. T. Callaghan, *Principles of Nuclear Magnetic Resonance Microscopy* (Oxford University Press, 1991).

3. B. O. Jimmink, M. Tessari, and A. P. M. Kentgens, "Hyphenation of 2D NMR With Hydrogenative PHIP," *Magnetic Resonance in Chemistry* 63 (2025): 278–282.

4. S. van Meerten, F. van Zelst, K. Tijssen, and A. Kentgens, "An Optimized NMR Stripline for Sensitive Supercritical Fluid Chromatography-Nuclear Magnetic Resonance of Microliter Sample Volumes," *Analytical Chemistry* 92 (2020): 13010–13016.

5. J. Bart, A. J. Kolkman, A. J. Oosthoek-de Vries, et al., "A Microfluidic High-Resolution NMR Flow Probe," *Journal of the American Chemical Society* 131 (2009): 5014–5015.

6. P. J. M. van Bentum, J. W. G. Janssen, and P. M. Kentgens, "Towards Nuclear Magnetic Resonance M-Spectroscopy and M-Imaging," *Analyst* 129 (2004): 793–803.

7. M. V. Gomez, S. Baas, and A. H. Velders, "Multinuclear 1D and 2D NMR With ^{19}F-Photo-CIDNP Hyperpolarization in a Microfluidic Chip With Untuned Microcoil," *Nature Communications* 14 (2023): 3885.

8. S. Baas and A. H. Velders, "Shim-Free Homebuilt 2 T Magnet for NMR Spectroscopy With Sub-ppm Resolution and Sub-Nanomole Sensitivity," *Research Square* (2023), https://doi.org/10.21203/rs.3.rs-3303984/v1.

9. M. V. Gómez, A. Juan, A. M. Rodríguez, et al., "Planar Microcoils for the Swift Optimization of Continuous-Flow Processes," SMASH Chamonix (2011).

10. R. M. Fratila and A. H. Velders, “Small-Volume Nuclear Magnetic Resonance Spectroscopy,” *Annual Review of Analytical Chemistry* 4 (2011): 227–249.

11. K. Göbel, O. G. Gruschke, J. Leupold, et al., “Phased-Array of Microcoils Allows MR Microscopy of Ex Vivo Human Skin Samples at 9.4 T,” *Skin Research and Technology* 21 (2015): 61–68.

12. V. Badilita, K. Kratt, N. Baxan, et al., “On-Chip Three Dimensional Microcoils for MRI at the Microscale,” *Lab on a Chip* 10 (2010): 1387.

13. S. B. Duckett and R. E. Mewis, “Application of Parahydrogen Induced Polarization Techniques in NMR Spectroscopy and Imaging,” *Accounts of Chemical Research* 45 (2012): 1247.

14. C. P. Slichter, *Principles of Magnetic Resonance* (Springer, 1996).

15. A. Abragam and M. Goldman, “Principles of Dynamic Nuclear Polarisation,” *Reports on Progress in Physics* 41 (1978): 395–467.

16. A. Abragam, *Principles of Nuclear Magnetism* (Oxford University Press, 1961).

17. I. Bertini, C. Luchinat, G. Parigi, and E. Ravera, *NMR of Paramagnetic Molecules—Applications to Metallobiomolecules and Models* (Elsevier, 2017).

18. L. Banci, I. Bertini, and C. Luchinat, *Nuclear and Electron Relaxation: The Magnetic Nucleus-Unpaired Electron Coupling in Solution* (Wiley-VCH, 1991).

19. L. Vander Elst, A. Roch, P. Gillis, et al., “Dy-DTPA Derivatives as Relaxation Agents for Very High Field MRI: The Beneficial Effect of Slow Water Exchange on the Transverse Relaxivities,” *Magnetic Resonance in Medicine* 47 (2002): 1121–1130.

20. S. Benders, M. Liauw, and B. Blümich, *MRI in Chemical Engineering* (Fachgruppe Chemie, Aachen, 2019).

21. B. Blümich, *NMR Imaging of Materials* (Clarendon Press; Oxford University Press, 2000).

22. F. Dalitz, L. Kreckel, M. Maiwald, and G. Guthausen, “Quantitative Medium-Resolution NMR Spectroscopy Under Non-Equilibrium Conditions Studied on the Example of an Esterification Reaction,” *Applied Magnetic Resonance* 45 (2014): 411–425.

23. L. von Damnitz and D. Anders, “A Review on the Mixing Quality of Static Mixers,” *ChemEngineering* 9 (2025): 128.

24. L. Kontschak, O. G. Gruschke, L. Trapp, et al., “MRI on Ion Exchange Resins at Different Length Scales,” *AIChE Journal* 71 (2024): e18659.

25. P. V. Danckwerts, “Continuous Flow Systems. Distribution of Residence Times,” *Chemical Engineering Science* 2, no. 1 (1953): 3857–3866.

26. N. Kockmann, *Transport Phenomena in Micro Process Engineering* (Springer Science & Business Media, 2007).